# An Experimental Study of Wheel–Rail Creep Curves Under Dry Contact Conditions Using V-Track

J. Krishnan, Gokul; Moraal, Jan; Li, Zili; Yang, Zhen

**DOI**
10.4203/ccc.7.2.5

**Publication date**
2025

**Document Version**
Final published version

**Published in**
Lubricants

**Citation (APA)**
J. Krishnan, G., Moraal, J., Li, Z., & Yang, Z. (2025). An Experimental Study of Wheel–Rail Creep Curves Under Dry Contact Conditions Using V-Track. *Lubricants*, *13*(7). https://doi.org/10.4203/ccc.7.2.5

*lubricants*

MDPI

*Article*

# An Experimental Study of Wheel–Rail Creep Curves Under Dry Contact Conditions Using V-Track †

**Gokul J. Krishnan, Jan Moraal, Zili Li and Zhen Yang ***

Section of Railway Engineering, Delft University of Technology, 2628 CN Delft, The Netherlands

* Correspondence: z.yang-1@tudelft.nl

† This paper is an extended version of our paper published in G. Jayasree Krishnan, Z. Yang, Z. Li, "Wheel/Rail Adhesion and Coefficient of Friction Measurement using Downscaled Test Rig", in J. Pombo, (Editor), "Proceedings of the Sixth International Conference on Railway Technology: Research, Development and Maintenance", Prague, Czech Republic, 1–5 September 2024, Civil-Comp Press, Edinburgh, UK, Online volume: CCC 7, Paper 2.5, 2024, https://doi.org/10.4203/ccc.7.2.5.

**Abstract**

Friction behaviour at the wheel–rail interface is of critical importance for railway operations and maintenance and is generally characterised by creep curves. The V-Track test rig was used in this study to measure both the lateral and longitudinal creep curves with uncontaminated dry interface conditions, utilising contact pressures representative of operational railway wheel–rail systems. The novelties of this study are threefold. 1. With proper representations of train/track components, the V-Track tests revealed the effects of structural dynamics on measuring wheel–rail creep curves in real life. 2. Pure lateral and longitudinal creepage conditions were produced with two distinct experimental principles—displacement- and force-controlled—on the V-Track, i.e., by carefully controlling the angle of attack and the traction/braking torque, respectively, and thus the coefficient of friction from lateral and longitudinal creep curves measured on the same platform could be cross-checked. 3. The uncertainties in the measured creep curves were analysed, which was rarely addressed in previous studies on creep curve measurements. In addition, the measured creep curves were compared against the theoretical creep curves obtained from Kalker's CONTACT. The influence of wheel rolling speed and torque direction on the creep curve characteristics was then investigated. The measurement results and findings demonstrate the reliability of the V-Track to measure wheel–rail creep curves and study the wheel–rail frictional rolling contact.

**Keywords:** coefficient of friction; creep curve; measurement; uncertainty analysis; rolling speed; torque direction

check for updates

Received: 15 May 2025

Revised: 13 June 2025

Accepted: 24 June 2025

Published: 26 June 2025

**Citation:** Krishnan, G.J.; Moraal, J.; Li, Z.; Yang, Z. An Experimental Study of Wheel–Rail Creep Curves Under Dry Contact Conditions Using V-Track. *Lubricants* **2025**, *13*, 287. https://doi.org/10.3390/lubricants13070287



## 1. Introduction

Characterisation of wheel–rail friction (or adhesion) is of great importance to the railway industry since it influences railway operations and maintenance. Railway vehicles depend on frictional forces at the wheel–rail contact for braking, traction, and guidance. Inadequate adhesion can extend stopping distances, potentially resulting in critical safety incidents, including signal overruns [1], and may result in wheel slips that damage rails and wheels and thus increase the maintenance cost. Friction forces (or creep forces) acting at wheel–rail interfaces originate from creep, i.e., the relative speed at the contact point between the wheel and the rail as rigid bodies [2], and may be affected by factors such as interface roughness [3], wheel rolling speed [4], normal load [4], and presence of third-body layers [1,5]. The variation of friction forces with creepage, i.e., the ratio of creep to wheel rolling speed, can be represented by a creep curve. Consequently, measurement of creep curves across varying interface conditions is fundamental to understanding friction phenomena at the wheel–rail contact.

While measurement of creep curves with operational trains on active tracks provides the most representative assessment of actual frictional conditions, such field-based experimental approaches typically involve excessive costs and contribute to accelerated rail degradation. Further, accurate measurement of creepage in either the longitudinal or lateral direction from a running train is extremely challenging. Longitudinal creepage calculation requires accurate measurements of both wheel rotational speed and train speed. Conventionally, wheel rotational speed measurements are performed using encoders on the wheel axles, which are subject to a wide range of error sources such as wheel slips, wheel wear, and hunting motion [6]. Train speed is usually obtained by measuring the rotational speed of non-driven axles [7]. However, the method is insufficiently accurate because wheel slip may also occur at the non-driven axles. Non-contact methods of train speed measurements such as eddy current-based sensors that detect rail clamps have been proposed, but even in the best situations, the relative expanded uncertainty of the method was around 1% [8]. All these factors result in poor accuracy of longitudinal creepage measurement [9]. Accurate lateral creepage measurement in the field is even more challenging, as the angle of attack (AoA) between the wheel and the rail is usually much less than $1^\circ$, especially on straight tracks. Measurements of Euler angles (roll, pitch, and yaw) of railway vehicles using onboard sensors and estimation algorithms (such as various types of Kalman filters and observers) have yielded accuracy in the range of $5^\circ$ [10]. Moreover, since it is difficult to control the wheel–rail contact conditions in the field, the influence of a particular parameter on the creep curve can hardly be separated from the others and assessed. Due to these reasons, creep curve measurements are often conducted in the laboratory under controlled conditions using either downscaled or full-scale test rigs. Twin-disc/roller rig setups have been commonly employed to generate longitudinal and lateral creep curves under different contact conditions [1,4,5,11–18] where the wheel and the rail are represented by two discs pressed together and driven by motors. By controlling the speeds of the discs, certain creep can be induced in the contact, and the resultant friction forces are measured and processed to obtain creep curves. However, these setups do not include representations of the track components below the rail such as rail pads, fasteners, and sleepers, or the vehicle components above the wheel such as the primary suspension of the rail vehicle. In the real-life wheel–rail contact, the stiffness and damping properties of these components can create structural vibrations which may affect the contact forces and creepages. Thus, the impact of real-life train/track dynamics on creep curve measurement is not captured by twin-disc/roller rig setups. Moreover, the curvature of the rail disc alters the shape of the contact patch compared to real-life contacts, where the rail curvature along the rolling direction of the wheel is infinite. This alters the pressure distribution and the distribution of stick and slip regions within the contact patch, which may thus affect the creep curve measurement. In addition, not many studies, besides [19], have provided uncertainty analysis for the creep curve measurement, and, to the authors' knowledge, studies that have measured both the longitudinal and lateral creep curves with a single test setup and then compared them are scarce.

This study investigated the wheel–rail creep curve using the V-track test rig, an innovative experimental facility developed for studies of the wheel–rail contact under controlled conditions [20–22]. By precisely scaling both geometry and loads [22], the V-Track reproduces an elliptical wheel–rail contact patch with identical levels of contact stresses to the real-life case. Furthermore, the test rig also incorporates scaled representations of track components (such as sleepers and fasteners) and vehicle components up to the primary suspension level, contributing to dynamic similarity [23] and enabling the evaluation of the impact of structural dynamics arising from these components. The test rig can accurately control the angle of attack and torque applied to the wheel, whereby wheel–rail contact with pure lateral creepage, pure longitudinal creepage, or a combination can be reproduced. In this study, we measured the pure lateral and pure longitudinal creep curves under clean and dry contact conditions in the V-Track using displacement-controlled and force-controlled experimental principles, respectively. We proposed a data processing method through which uncertainty limits for the measured creep curve can be derived. The influence of wheel rolling speed and torque direction, i.e., traction or braking on the creep curve characteristics were then investigated. The measured lateral and longitudinal creep curves were compared with Kalker's CONTACT solutions, and also cross-checked with each other in terms of the coefficient of friction (CoF) to show the reliability of creep curve measurement using the V-Track. Selected results from this study were presented in [24].

## 2. Materials and Methods

### *2.1. V-Track Test Rig*

The V-Track test rig consists of a ring track on which a maximum of 4 wheels can roll, as shown in Figure 1a. The ring track comprises four pieces of rails (rail 1, rail 2, rail 3, and rail 4) with the standard S7 profile that are each bent into an arc covering 90 degrees and connected by joints. The rails are fixed onto 100 equally spaced sleepers throughout the circumference of the ring track using fasteners. Rail pads are placed between the rails and the sleepers. To achieve dynamic similarity to the real-life track structure, rubber pads are laid underneath the sleepers to represent the stiffness and damping of the ballast layer. In the configuration used for the present work, only two wheels are present, W1 and W2, as shown in Figure 1a. The scaled wheels are connected to a set of two vertical springs through an axle box and a guiding block. These components constitute the wheel assemblies, as shown in Figure 1b. The springs are compressed to provide the desired vertical forces to the wheel–rail contact and play the role of the primary suspension of a rail vehicle. The wheel assemblies are connected to the platform shown in Figure 1a through a steel frame. A motor drives the platform, pulling the wheel assemblies to travel along the ring track. The direction of rotation is clockwise from a top view (as shown in Figure 1a). Additionally, the wheels are also connected to a second torque motor through drive shafts, which can apply braking or traction torques to the wheels. The AoA between the wheel and the rail can be varied by rotating the wheel and the axle box around the axle box pivot, and is measured using a dial gauge mounted to the guiding block that indicates the distance rotated by a steel beam attached to the axle box, as shown in Figure 1c. The steel beam has a length of 68.45 mm corresponding to a rotation angle of ca. 0.08° for every 1 mm of the dial gauge reading. For each wheel assembly, a four-sensor piezoelectric dynamometer is placed between the wheel assembly and the steel frame, which measures the wheel–rail contact forces in three directions [21]. The directions of the measured contact forces and wheel torque are indicated by green arrows in Figure 1b. The wheel rolling speed is controlled to a constant value by setting the rotational speed of the platform in the control software. The braking or accelerating torque applied to the wheel can also be controlled and measured by a torque sensor placed in line with the wheel drive shaft. The torque sensor also has an integrated optical incremental encoder that measures the rotational speed of the wheel. The main technical parameters of the V-Track test rig are provided in Table 1, and a more detailed description of its design and contact force measurement capabilities can be found in [20] and [21], respectively.

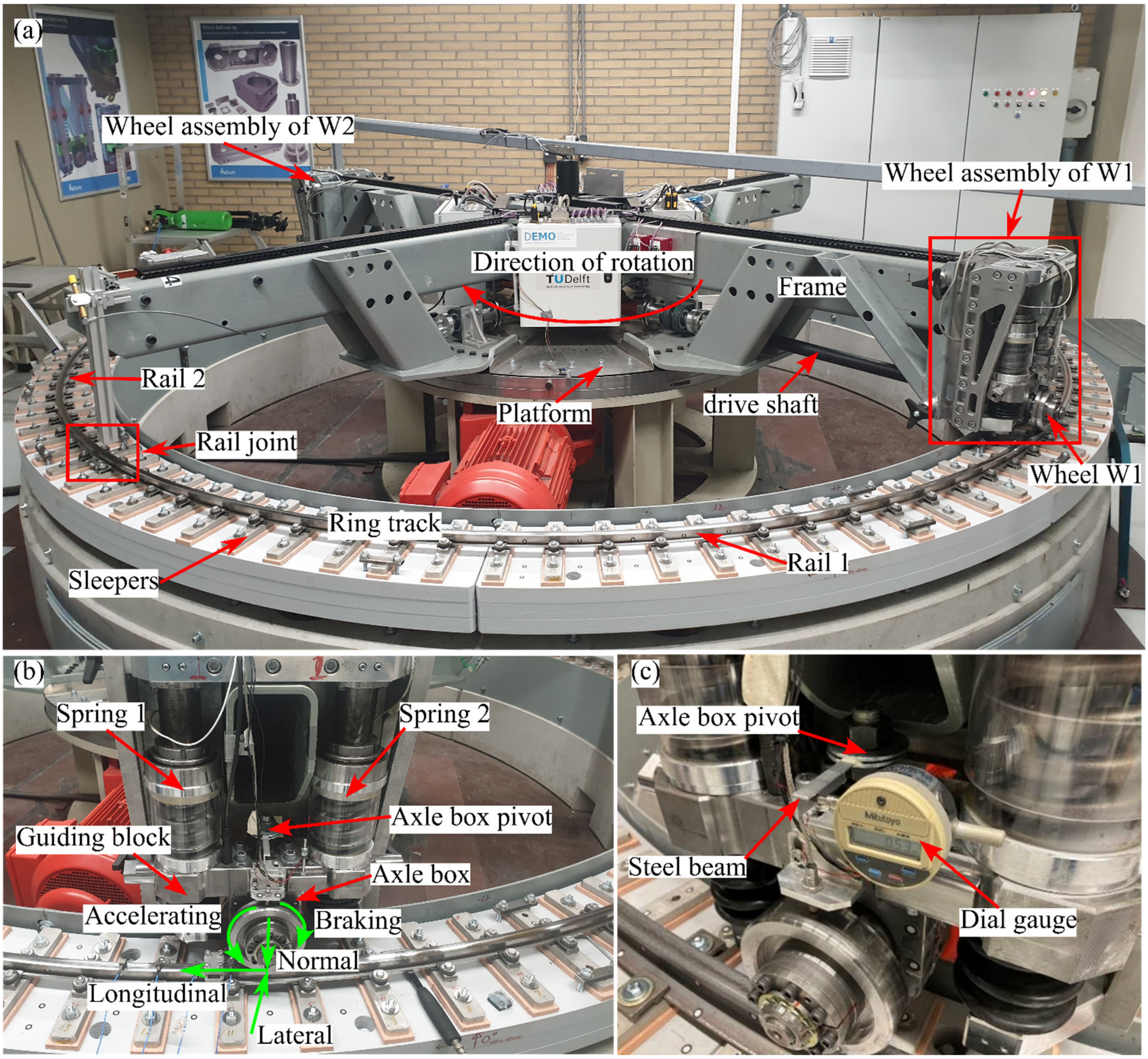


**Figure 1.** The structure of the V-Track test rig: (**a**) an overview of the V-Track; (**b**) a close-up of a wheel assembly; (**c**) the AoA measurement setup.

**Table 1.** Main technical parameters of the V-Track test rig.

| Parameter | Value/Range |
|---|---|
| Ring track diameter | 4.0 m |
| Wheel diameter | 130 mm |
| Wheel translational speed | up to 40 km/h |
| Wheel normal load | up to 7500 N |
| Wheel angle of attack | between −2 and 2 degrees |
| Wheel torque | between −500 and 500 N·m |
| Data sampling frequency | 16,670 Hz |

*2.2. Test Procedure*

The lateral and longitudinal creep curve measurements conducted in this study, with a total of nine test cases, are summarised in Table 2. Before running the tests, the vertical rail alignment was adjusted to within ± 5 mm, so that the normal force on the rolling wheel would remain relatively constant throughout the circumference of the ring track. The nominal normal load for the two wheels in the current study was set to 2600 N, which would give an elliptical contact patch with semi-axes of 1.068 mm and 1.012 mm and a maximum contact pressure of 1.2 GPa, which corresponds well to the wheel–rail contact pressure experienced in the Dutch railway. To accurately control the braking and accelerating torque, only one out of the two wheels, wheel 1 (W1), was connected to the wheel torque motor. The other wheel, wheel 2 (W2), was allowed to roll freely by disconnecting it from the wheel torque motor and only being pulled by the steel frame.

**Table 2.** Test codes and their respective test conditions.

| Test Code | Type of Test | Wheel Rolling Speed |
|---|---|---|
| Test 1 v4 | Lateral | 4 km/h |
| Test 1 v8 | Lateral | 8 km/h |
| Test 1 v16 | Lateral | 16 km/h |
| Test 2 v4 | Longitudinal, braking | 4 km/h |
| Test 2 v8 | Longitudinal, braking | 8 km/h |
| Test 2 v16 | Longitudinal, braking | 16 km/h |
| Test 3 v4 | Longitudinal, accelerating | 4 km/h |
| Test 3 v8 | Longitudinal, accelerating | 8 km/h |
| Test 3 v16 | Longitudinal, accelerating | 16 km/h |

#### 2.2.1. Lateral Creep Curve Test

For the lateral creep curve test (Test 1 in Table 2), a small traction torque was applied to W1 to neutralise the braking torque arising from friction in the wheel bearings, which thus caused a nominal-zero longitudinal wheel–rail contact force, such that pure lateral creepage contact conditions could be maintained. The AoA was increased gradually from 0.0°. The angle increment was initially in a step of 0.08°, and reduced to 0.04° after an AoA of 0.32° to capture more data points of the creep curve when approaching saturation. For each angle step, the wheel–rail contact forces were measured for at least three ring track cycles. The AoA was increased until friction saturation was observed, when the recorded lateral force level was found to remain approximately constant with a further increase in the AoA. When friction saturation was achieved, the coefficient of adhesion (CoA) could be approximated as the CoF of the V-Track. The interfaces of the rails and wheels were carefully cleaned with acetone before each AoA increment to maintain clean and dry contact conditions throughout the test. At each angle step, three rolling speeds of the wheel were tested, namely, 4 km/h, 8 km/h, and 16 km/h.

#### 2.2.2. Longitudinal Creep Curve Test

For the longitudinal creep curve tests (Test 2 and Test 3 listed in Table 2), the wheel AoA was set as close as possible to zero to produce pure longitudinal creepage contact conditions. The braking torque applied to W1 was increased gradually from zero. The torque increment was set to 20 N·m initially, until a torque of 60 N·m, and then reduced to 3 N·m until friction saturation was achieved. The creep curve close to friction saturation could thus be more accurately captured. For each torque step, the wheel–rail contact forces and the wheel and platform rotational speeds were recorded for at least three cycles to guarantee test repeatability. After three torque steps, the interfaces of the rails and wheels were cleaned with acetone to maintain clean and dry contact conditions throughout the test. The same procedure was repeated for the tests with the traction or accelerating torque applied. Both braking and accelerating torque tests were conducted at three wheel rolling speeds of 4 km/h, 8 km/h, and 16 km/h.

### 2.3. Data Processing and Uncertainty Analysis

When measuring creep curves, creepage and the corresponding CoA need to be obtained. Data processing in this subsection involves the calculations of lateral and longitudinal creepage and the CoA. An uncertainty analysis of these quantities in the measurement was also carried out. In the subsequent sections, the data measured from rail 2 are used as a representative example, as the best control of torque and the AoA was achieved for rail 2. The measurements on the other three rails exhibited similar trends.

#### 2.3.1. Calculation of Lateral Creepage

Lateral creepage $\xi_y$ was approximated as the AoA, considering the AoA was small, which was measured using a dial gauge, as in Equation (1):

$$\xi_y = sin(AoA) = sin\left(\frac{d}{L}\right), \tag{1}$$

where $d$ is the reading from the dial gauge and $L$ is the length of the steel beam (Figure 1c). The uncertainty in measuring lateral creepage can be obtained through type B evaluation by applying the law of propagation of uncertainty [25] to Equation (1). This gives the following:

$$var(\xi_y) = \left(\frac{1-\xi_y^2}{L^2}\right)var(d) + \left(\frac{\left(1-\xi_y^2\right)d^2}{L^4}\right)var(L), \tag{2}$$

where $var(X)$ stands for the variance of $X$. The variance in $d$ and $L$ corresponds to errors in the measurement of the dial indicator and the steel beam length at the dial indicator contact point. These are modelled as rectangular distributions with limits equal to the resolutions of the instruments used for the measurements. The resolution of the dial gauge is 0.01 mm, that of the calipers used for the measurement of the length of the steel beam—0.02 mm. The standard uncertainty in the measurement of lateral creepage is the square root of the variance. The maximum standard uncertainty in the lateral creepage measurement in this study can thus be calculated via Equation (2) as 0.00422%.

#### 2.3.2. Calculation of Longitudinal Creepage

In the V-track, longitudinal creepage $\xi_x$ can be calculated as per Equation (3):

$$\xi_x = \frac{|\Omega R_p - \omega R_w|}{\Omega R_p}, \tag{3}$$

where $\Omega$ is the platform rotational speed, $\omega$ is the wheel angular speed, $R_p$ is the radius of the ring track, and $R_w$ is the radius of the wheel. However, in the current V-track configuration, the encoder used to measure the platform rotational speed has a significantly lower resolution, and thus a larger error, than the encoder measuring the wheel angular speed, which may lead to a large error in the calculated longitudinal creepage. To overcome this, another approach is used in this study for the calculation of longitudinal creepage, where only the wheel angular speed measurement is required, as given by Equation (4):

$$\xi_x = \frac{|\omega_0 R_w - \omega R_w|}{\omega_0 R_w} \tag{4}$$

Here, $\omega_0$ represents the wheel angular speed measured with a nominal-zero longitudinal wheel–rail contact force, i.e., the wheel–rail contact is in a free rolling condition. Because the wheel circumferential speed $\omega_0 R_w$ is theoretically equal to the wheel rolling speed

$\Omega R_p$ in the free-rolling condition, and the platform rotational speed $\Omega$ is kept nominally constant during each longitudinal test case, $\omega_0 R_w$ can be used in place of $\Omega R_p$.

An example of the wheel angular speed measured with the wheel encoder is shown in Figure 2 in the free-rolling condition of Test 2 v8. The bottom horizontal axis represents the angular position of W1 as it rolls along the circumference of the test rig, and the top horizontal axis marks the sleeper numbers. The fluctuations of the signal, i.e., high-frequency variations superimposed on a low-frequency wave, are induced by two types of errors of the optical incremental encoder used for wheel speed measurement: short-term errors (also called differential non-linearities), which manifest as high-frequency random fluctuations in the measured speed signal, and long-term errors (also called integral non-linearities) that are more prominent at lower frequencies [26,27]. Before the calculation of longitudinal creepage using Equation (4), the wheel speed signal has to be processed to reduce the impact of these error sources.

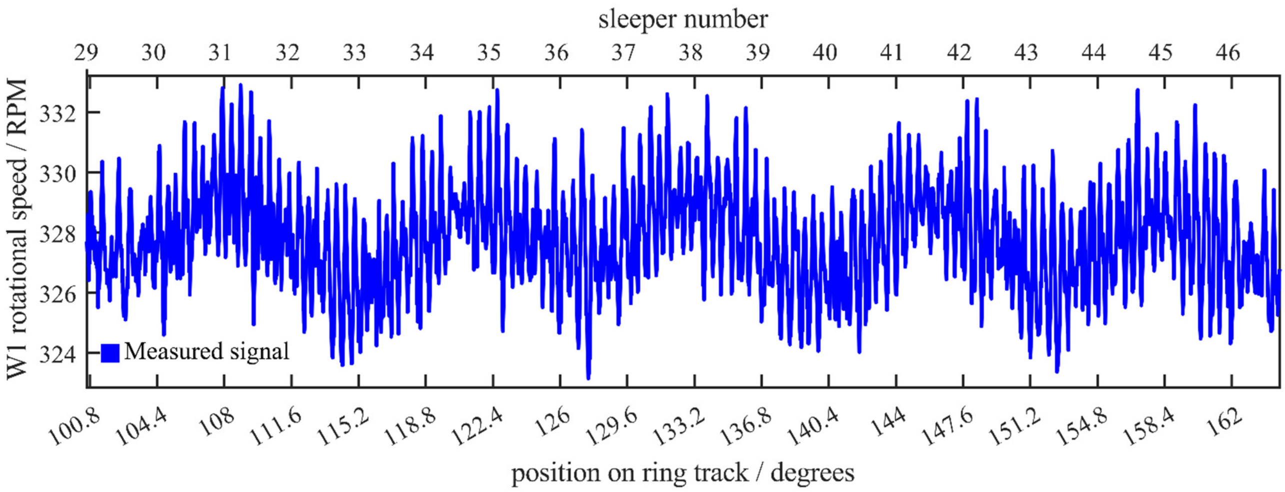


**Figure 2.** Wheel angular speed signal measured from the encoder.

Reducing Short-Term Errors

Short-term errors are mainly caused by the internal processes within the encoder and are specified by the cycle error of the encoder. This cycle error is the difference between the ideal angle turned in one encoder cycle (given by $\frac{360°}{N}$, where N is the number of pulses or counts per revolution of the encoder) and the actual angle covered [28]. Since short-term errors are random in nature, their influence can be reduced by averaging. The number of datapoints to be averaged can be determined based on the cycle error specifications of the encoder and the required uncertainty in longitudinal creepage, through a type B modelling of the uncertainty in longitudinal creepage.

Applying again the law of propagation of uncertainty to Equation (4), we can write the variance in the longitudinal creepage as follows:

$$var(\xi_x) = 2(1-\xi_x)^2 \frac{var(\omega)}{\omega^2} \tag{5}$$

The V-Track uses the period-based method (or T-method) to calculate the wheel rotational speed, where the time period for a certain number n of encoder pulses is measured using a high-resolution clock signal [29]. In this method, the wheel rotational speed is calculated as follows:

$$\omega = \frac{n\Delta\theta}{\Delta t}, \tag{6}$$

where $\Delta\theta$ is the angle turned by the encoder in one pulse and $\Delta t$ is the elapsed time. For an ideal encoder, $\Delta\theta = \frac{360^\circ}{N}$. However, for a real encoder, the angle turned can be modelled as follows:

$$n\Delta\theta = \frac{360n}{N} + \delta\theta, \tag{7}$$

where $\delta\theta$ is the zero mean variable which denotes the difference in the angle turned due to the cycle error of the encoder. By substituting $n\delta\theta$ in Equation (6) with Equation (7), and applying the law of propagation of uncertainty once again, we obtain the following:

$$\frac{var(\omega)}{\omega^2} \approx \frac{var(\delta\theta)}{(n\Delta\theta)^2}, \tag{8}$$

where $var(\delta\theta)$ is the variance caused by the cycle error of the encoder and can be obtained from the encoder specifications. Here, we neglected the influence of uncertainty in the time measurement. The V-Track uses a high-accuracy field-programmable gate array (FPGA) clock with uncertainties of the order of 200 ppm, whose error is insignificant compared to the error in the angle measurement. Substituting Equation (8) in Equation (5) and rearranging, we obtain an expression for the angle turned by the encoder:

$$(n\Delta\theta)^2 = \frac{2(1-\xi_x)^2}{var(\xi_x)} var(\delta\theta) \tag{9}$$

For the V-Track, the encoder specifications state a maximum cycle error ($\delta\theta_{max}$) of 0.0104° and a typical cycle error ($\delta\theta_{typ}$) of 0.004166° [30]. Thus, for the V-Track, $\delta\theta$ can be modelled as a trapezoidal distribution, whose variance is as follows:

$$var(\delta\theta) = \frac{\delta\theta_{max}^2}{6}\left(1 + \left(\frac{\delta\theta_{typ}}{\delta\theta_{max}}\right)^2\right) \tag{10}$$

Now, from Equations (9) and (10), we can find the value of $n\delta\theta$, for which a certain level of uncertainty in creepage is maintained. In this study, we set the limit for expanded uncertainty covering 95% of longitudinal creepage values as 0.15% for a nominal value of 1%. With this assumption, the variance of longitudinal creepage can be set as follows:

$$var(\xi_x) = \left(\frac{0.15}{2 * 100}\right)^2 = 5.625 \cdot 10^{-7} \tag{11}$$

From Equations (9) and (11), $n\delta\theta$ is found to be 8.54°, which is rounded up to 10°. This means that if the wheel rotational speed is measured in an interval of 10° of wheel rotation, the uncertainty of the resultant longitudinal creepage is within the specified limit, assuming that the true wheel angular speed has not changed during this interval. Using this value, a low-pass resampling filter is applied to the measured wheel speed signal. The filtered signal and the original signal are compared in Figure 3, where the reduction in high-frequency variations can be clearly observed.

Reducing Long-Term Errors

As shown in Figure 3, a low-frequency fluctuation is also present in the measured wheel speed signal. The Fast Fourier transform (FFT) of the resample-filtered signal in Figure 3 is plotted in Figure 4, where we can see that the main contribution is from the 5.53 Hz frequency, very close to the nominal wheel rotational frequency of 5.44 Hz. This can be due to the eccentricity of the encoder mounting [31]. When the encoder shaft is not completely aligned with the wheel shaft, the centre of the code wheel inside the encoder is offset from the rotational centre of the wheel shaft, causing a periodic disturbance in the measured wheel speed, at the frequency of rotation. To reduce the influence of this error, a notch filter is applied to the filtered signal at the frequency of wheel rotation and its second harmonic. The resultant wheel speed signal is shown in Figure 5, compared to the resample-filtered signal from the previous step (reducing only short-term errors). We may see that the influence of long-term errors is mostly reduced. This notch-filtered signal was finally used in Equation (4) as the measured wheel angular speed $\omega$ to calculate the longitudinal creepage.

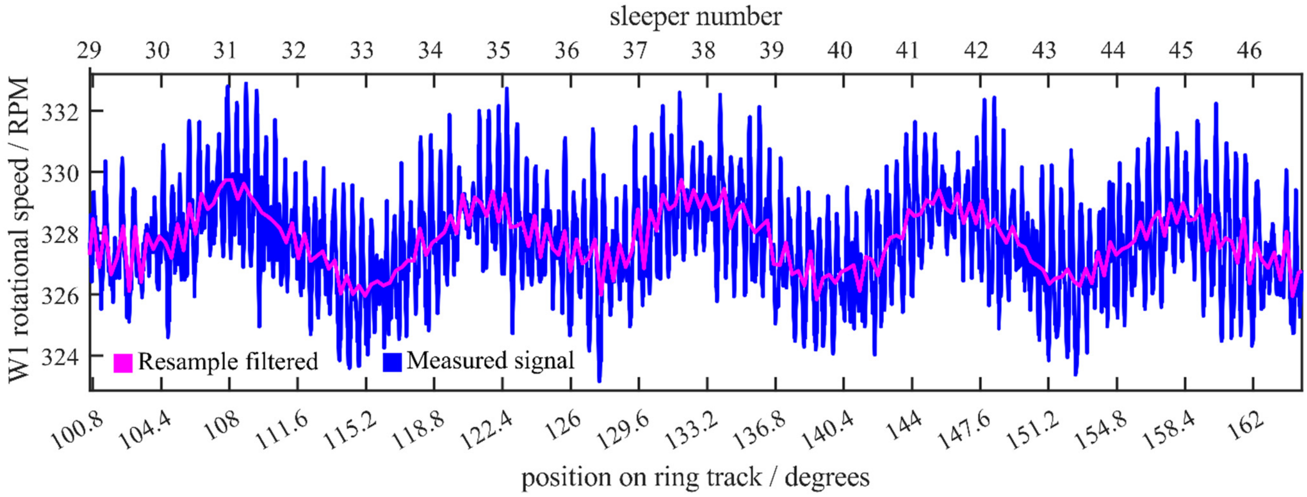


**Figure 3.** Comparison of the measured angular speed signal and the resample-filtered angular speed signal.

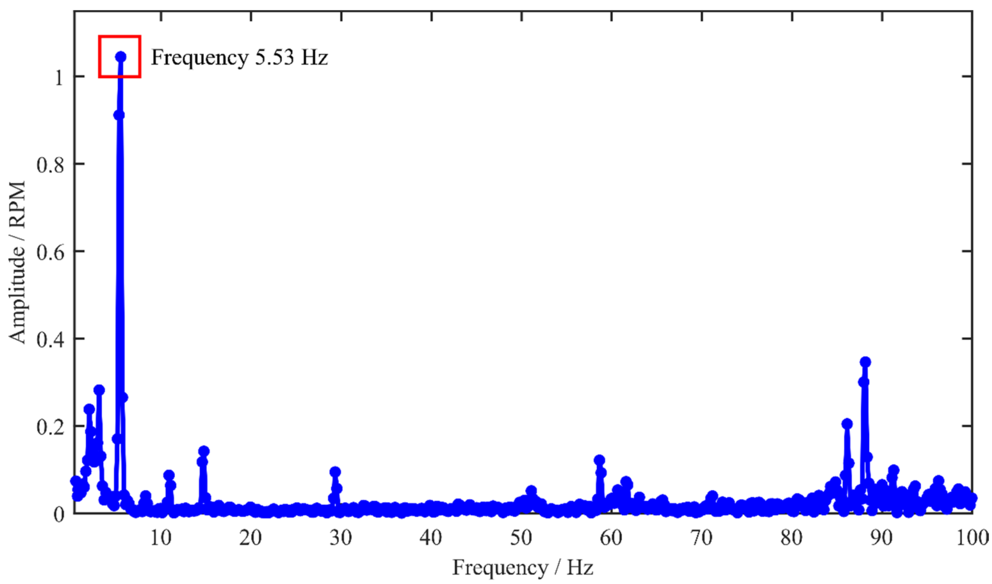


**Figure 4.** FFT of the resample-filtered wheel speed signal.

The increase in the calculated longitudinal creepage with applied torque can be visualised in Figure 6, where the average values of $\omega R_w$ are compared to $\omega_0 R_w$ across increasing values of braking and accelerating torques. We can clearly see the increase in slip speed and creepage from the diverging values between $\omega_0 R_w$ and $\omega R_w$.

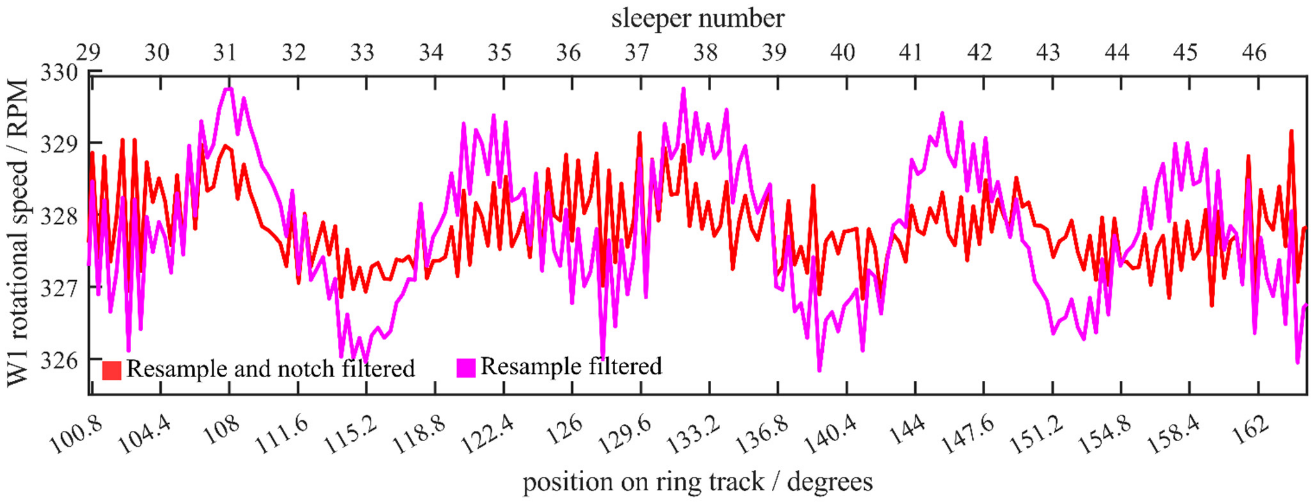


**Figure 5.** Comparison of the resample-filtered angular speed signal and the resampled and notch-filtered angular speed signal.

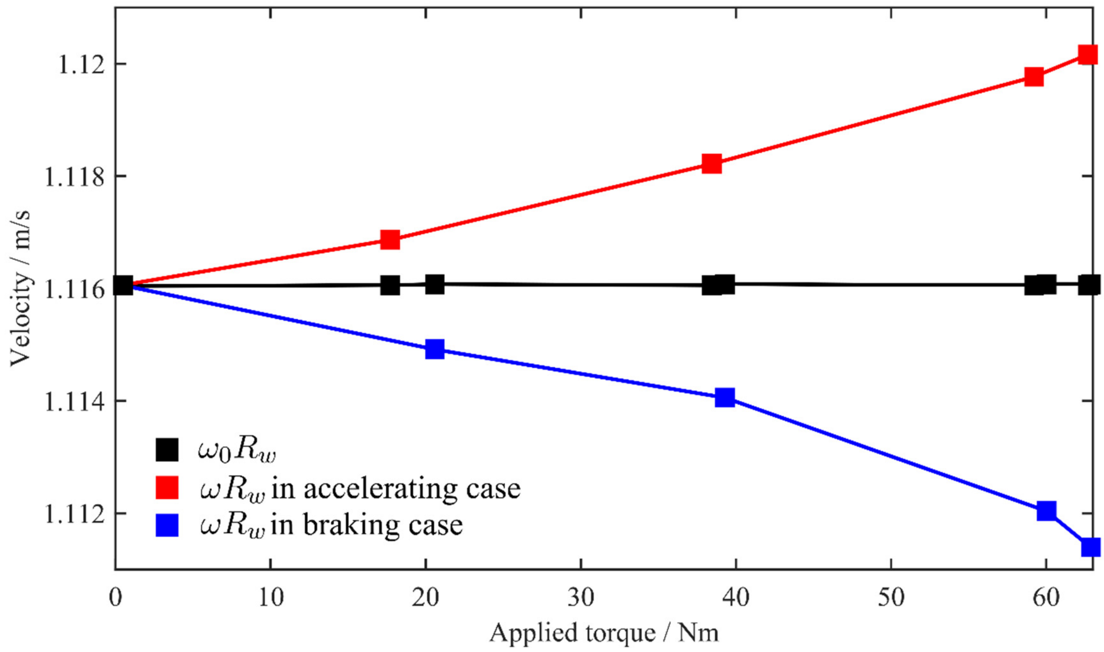


**Figure 6.** Visualisation of increasing longitudinal creepage with torque; $\omega_0 R_w$ stays constant throughout the increasing applied torque, while $\omega R_w$ diverges from $\omega_0 R_w$ in opposite directions for accelerating and braking torques.

### 2.3.3. Calculation of the CoA

The CoA in each test case was calculated based on the measured longitudinal, lateral, and normal contact forces via Equation (12):

$$CoA = \frac{\sqrt{F_x^2 + F_y^2}}{F_z}, \tag{12}$$

where $F_x$, $F_y$, and $F_z$ are the longitudinal, lateral, and normal contact forces. Figure 7 plots the contact forces measured in the lateral creep curve test (Test 1 v8). The last three AoA cases (i.e., AoA = 0.41°, 0.046°, and 0.50°, all beyond friction saturation) were removed to improve readability. The saturation of lateral force can be observed in the final few cases when the $AoA \geq 0.24$, as no increase was observed with a further increase of the AoA. By carefully adjusting the vertical rail alignment along the ring track to within ± 5 mm, the mean value of the normal force, consistent for all the AoA cases, was maintained within 2661.7 ± 20 N. The mean value of the longitudinal force was maintained within 5.7 ± 10 N so that the contact could be considered under pure lateral creepage conditions.

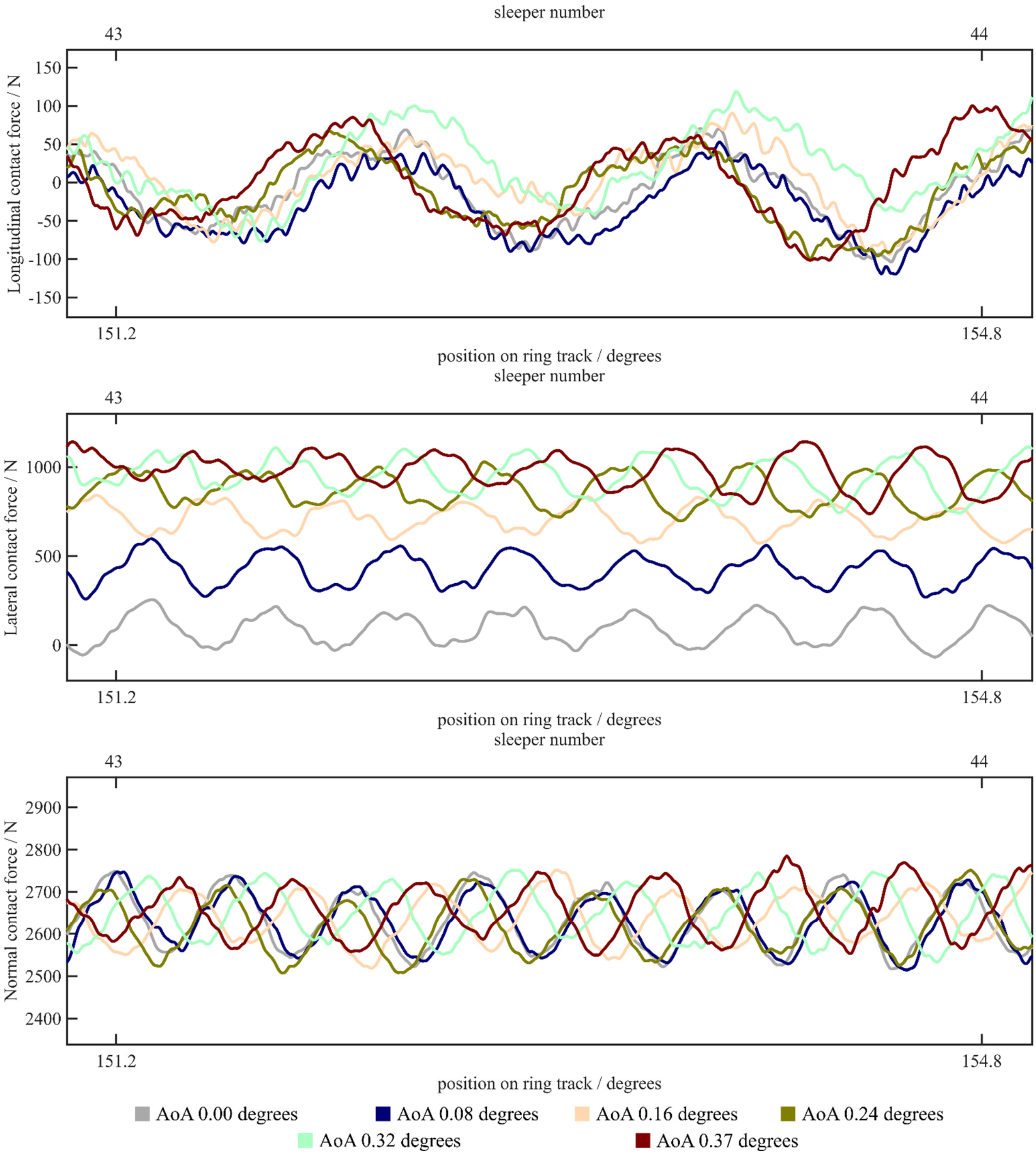


**Figure 7.** Measured contact forces across the tested AoA range in Test 1 v8.

Figure 8 plots the time histories of the contact forces measured in the longitudinal creep curve test (Test 2 v8). The last torque case (i.e., 69 N·m) was removed to improve readability. The saturation of the longitudinal contact force is visible when the torque is over 63 N·m. The mean value of the lateral force was maintained within 66 ± 47.6 N, which at the maximum value was less than 11% of the maximum longitudinal force at saturation. The contact could thus be considered under pure longitudinal creepage conditions.

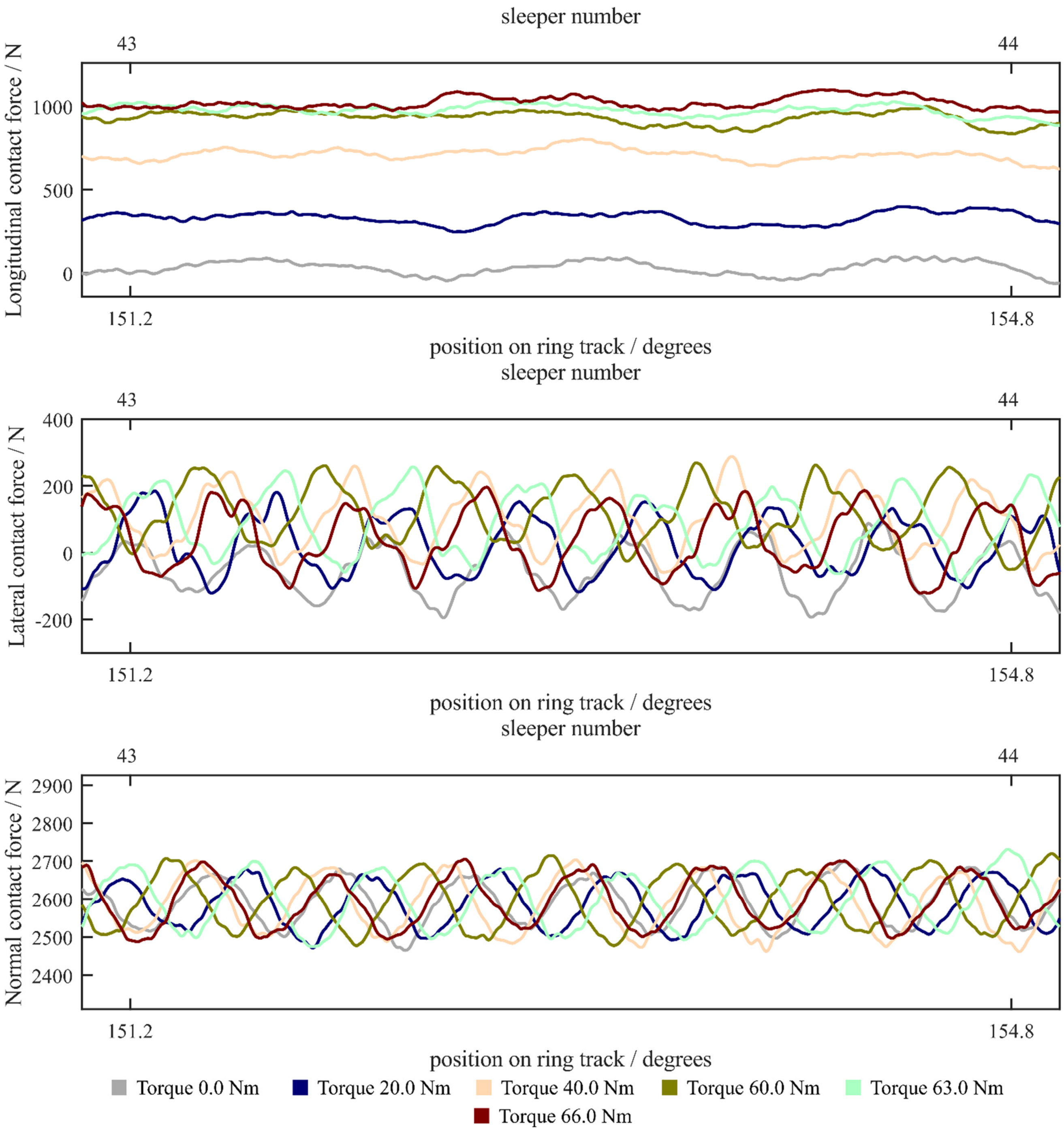


**Figure 8.** Measured contact forces across the tested torque range in Test 2 v8.

To plot the creep curves, i.e., the CoA given as a function of creepage, a representative value of the CoA needs to be calculated from the measured wheel–rail contact force time histories at each creepage level. In this study, we used the average value of the measured forces, based on which a representative CoA was calculated, as in [1,32,33]. The uncertainty of the calculated CoA points can be approximately quantified through type B evaluation. An application of the law of propagation of uncertainty to Equation (12) provides the following:

$$var(CoA) = \left(\frac{F_x}{CoA * F_z{}^2}\right)^2 var(F_x) + \left(\frac{F_y}{CoA * F_z{}^2}\right)^2 var(F_y) + \left(\frac{CoA}{F_z}\right)^2 var(F_z) \quad (13)$$

The variances in the measured contact forces can be calculated from a static calibration of the dynamometer as provided in [21], where the error of the dynamometer was estimated to be 0.95% for $F_x$, 4.38% for $F_y$, and 0.96% for $F_z$. The calibration was performed with a load cell, which itself has an error of 0.6%. Combining these error values, we obtain the following:

$$\begin{aligned} var(F_x) &= \left(\frac{0.95F_x}{300}\right)^2 + \left(\frac{0.6F_x}{300}\right)^2, \\ var(F_y) &= \left(\frac{4.38F_y}{300}\right)^2 + \left(\frac{0.6F_y}{300}\right)^2, \\ var(F_z) &= \left(\frac{0.96F_z}{300}\right)^2 + \left(\frac{0.6F_z}{300}\right)^2, \end{aligned} \tag{14}$$

where the errors in the forces measured by the dynamometer and the load cell were modelled as normal distributions with expanded uncertainty to 99% coverage values equal to the error values obtained from static calibration. Using Equations (13) and (14), the approximate uncertainty at every CoA point on the creep curve can be calculated. The maximum standard uncertainty in the CoA in the lateral and longitudinal creep curve tests was 0.006 and 0.002, respectively.

## 3. Results and Discussion

With the processed creepage and CoAs, the lateral and longitudinal creep curves could be obtained for all the test cases in Table 2. To account for any deviation of the CoF along a rail of the V-Track, each rail was divided into five divisions, and the creep curves were plotted for each division. The creep curves were then compared across wheel rolling speed conditions, between the opposite directions of the applied torque, and with the theoretical creep curves obtained from the widely-accepted Kalker's CONTACT programme [2]. Finally, the lateral and longitudinal creep curves were also cross-checked, demonstrating the reliability of the V-Track in studying wheel–rail frictional rolling contact.

### 3.1. Lateral Creep Curves

#### 3.1.1. Measured Creep Curves

The lateral creep curves obtained from Test 1 v8 for each rail division, as well as a comparison, are shown in Figure 9. At each datapoint in the creep curve, the vertical blue error bar denotes the variation in the CoA measured in the three repeated cycles at that creepage point. The error bar length corresponds to 20 times the standard deviation of the measured CoA values. Although such a high multiplier of the standard deviation was used to increase legibility, the error bars are still of short length in the figure, denoting excellent repeatability of the CoA measurement. Additionally, at each point in the plotted creep curve, a shaded orange region represents the expanded uncertainty of that point to 95% coverage. The width of the orange region represents the uncertainty in the lateral creepage measurement calculated via Equation (2), while the height represents the uncertainty in the CoA measurement, calculated via Equations (13) and (14). Connecting the corners of the shaded regions, two black dashed curves were drawn, indicating the bounds of the overall uncertainty in the measured creep curve at 95% coverage. The maximum value of the creep curve, or the CoA, represents the CoF. The CoF values of all five divisions were found to be very close to each other, with an average of 0.3823 and a standard deviation of 0.0092. This indicates an approximately constant CoF along the rail. The CoF measured from the lateral creep curve test was then used for the estimation of the maximum torque applied in the longitudinal tests to avoid severe interface damage induced by high longitudinal creepage.

As can be observed from Figure 9, the measured lateral creep curves did not start at zero, i.e., the measured CoAs were non-zero at the zero creepage. This could be due to the existence of a small AoA in the V-Track setup, which can hardly be avoided and causes a small lateral force. Note that the influence of this small AoA on the measured creep curves was limited, mainly on the starting point, which can be confirmed by comparisons with CONTACT solutions later Section 3.1.3.

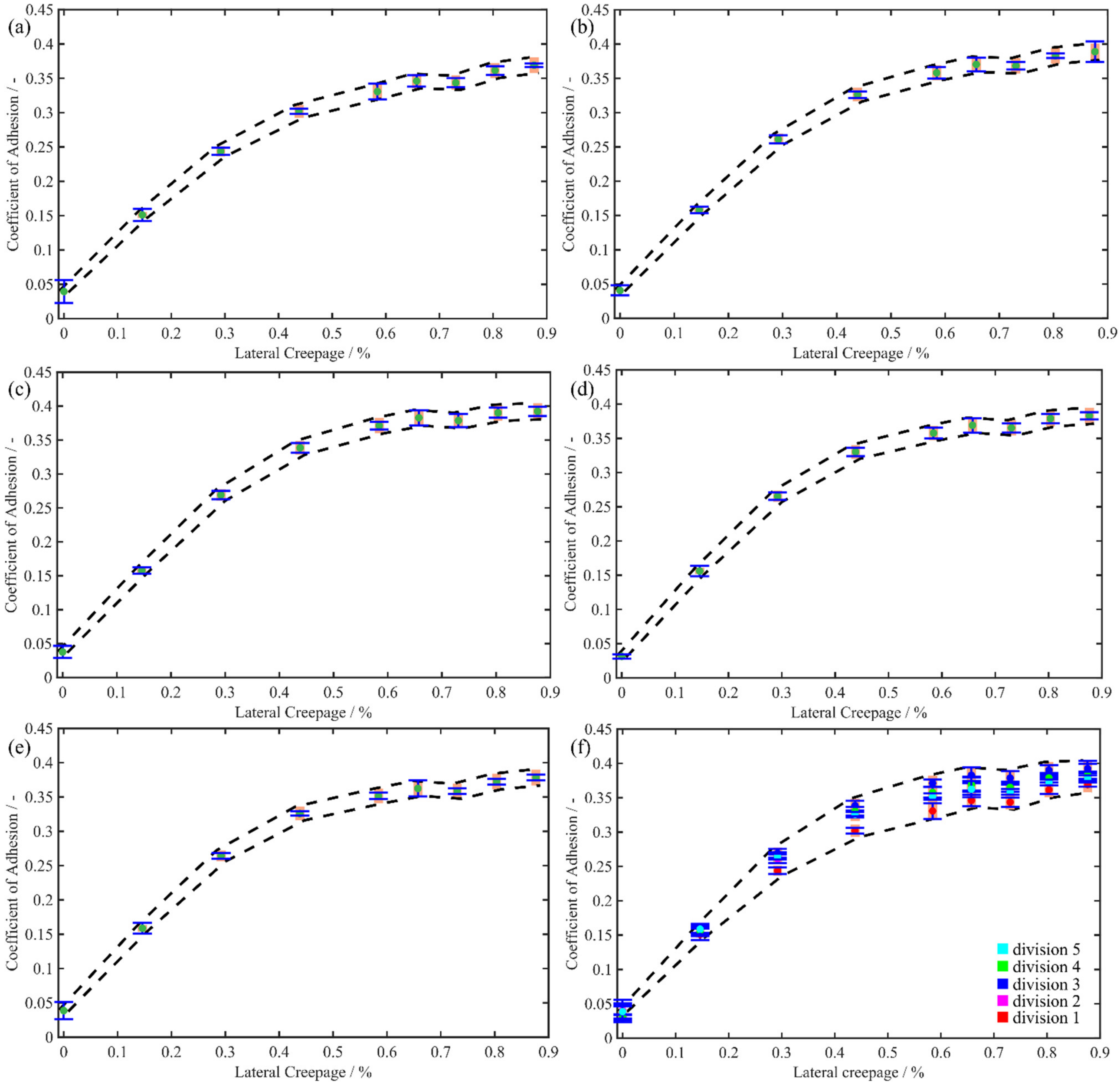


**Figure 9.** Lateral creep curves for Test 1 v8: (**a**) division 1; (**b**) division 2; (**c**) division 3; (**d**) division 4; (**e**) division 5; (**f**) comparing creep curves of all divisions.

### 3.1.2. Influence of the Rolling Speed

The combined creep curves, i.e., plotted on the basis of the measurement results from all five rail divisions, for Test 1 v4, Test 1 v8, and Test 1 v16 are compared in Figure 10. The uncertainty bounds and error bars were omitted for the sake of legibility. The influence of the wheel rolling speed on the measured creep curves can be identified in two aspects: a slight decrease in the CoF value and a reduction of the creep coefficient, i.e., the initial slope of the creep curve. A reduction of the CoF with an increase in rolling speed in the lateral creep curve was reported in [18]. In this study, the CoF reduced from 0.4021 for 4 km/h to 0.3822 for 16 km/h of the wheel rolling speed. The dashed lines in Figure 10 represent the best linear fits of the datapoints in the least-squares error sense, corresponding to the first three lateral creepage values for each tested speed. The slope of the dashed line is thus an estimate of the creep coefficient. In this study, the creep coefficient reduced from 0.7970 $\%^{-1}$ for 4 km/h to 0.7501 $\%^{-1}$ for 16 km/h. A change in the creep coefficient was observed in an experimental study of the influence of various third-body layers on the creep curve characteristics [34]. In this study, as mentioned in Section 2.2.1, the lateral creep curves with three rolling speeds, from low to high, were continuously tested in one go without stopping the test rig. Some debris of the wheel/rail material may act as a third-body layer at the wheel–rail interface for the higher speed test cases, which was responsible for the observed reduction in the creep coefficient.

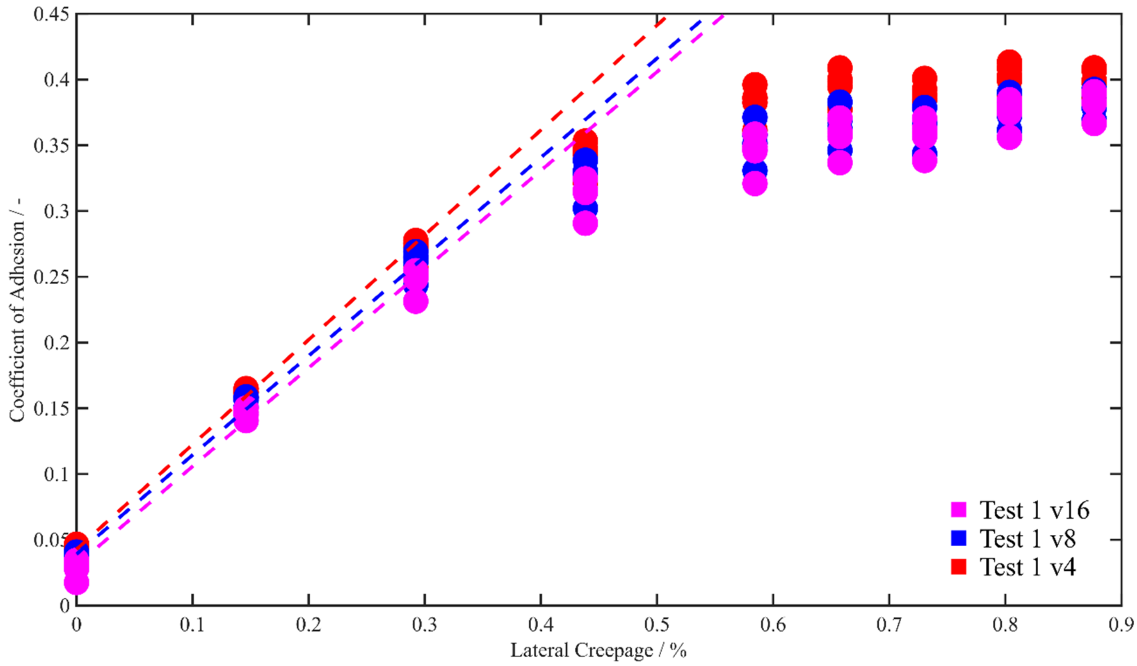


**Figure 10.** Comparison between the lateral creep curves across the tested speeds. The dashed lines represent the estimated creep coefficients for each test case.

### 3.1.3. Comparison with CONTACT

The measured lateral creep curves for each speed were then compared with the theoretical lateral creep curves obtained with the CONTACT programme in Figure 11. The theoretical creep curves were obtained based on the measured CoF values and the normal loads. A Poisson's ratio of 0.27 and a shear modulus of 82.7 GPa were used as the material properties.

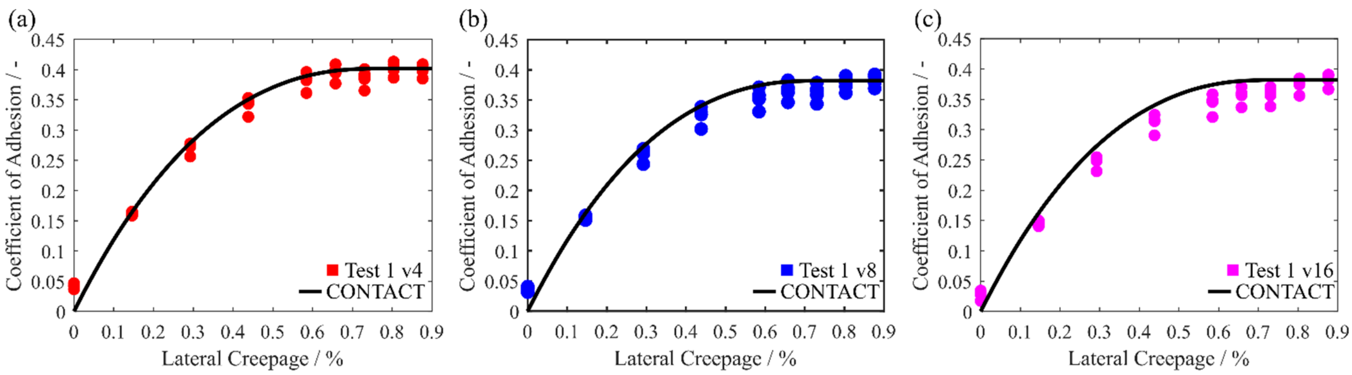


**Figure 11.** Comparison between the measured lateral creep curves and the numerical lateral creep curves from Kalker's CONTACT: (**a**) Test 1 v4; (**b**) Test 1 v8; (**c**) Test 1 v16.

We can see an excellent agreement between the experimental and theoretical creep curves for Test 1 v4, as shown in Figure 11a. The only outlier is the starting point, and the cause is discussed in Section 3.1.1. The reduction in the creep coefficient caused small discrepancies between the measured and simulated creep curves for Test 1 v8 and Test 1 v16, since the applied CONTACT programme does not consider the effect of third-body layers. The good agreement between the measurements and simulations demonstrates the V-Track test rig as a reliable and accurate tool for wheel–rail lateral creep curve measurements.

### *3.2. Longitudinal Creep Curves*

#### 3.2.1. Measured Creep Curves

The longitudinal creep curves obtained from Test 2 v8 (under wheel braking) for five rail divisions, as well as a comparison thereof, are shown in Figure 12. The vertical and horizontal error bars denote the variations in the CoA and longitudinal creepage measured in the three repeated cycles at each torque value. The error bar length in the vertical direction corresponds to 20 times the standard deviation of the measured CoA values, while the error bar length in the horizontal direction corresponds to twice the standard deviation of the measured longitudinal creepage values. As in the lateral creep curve, the shaded orange regions corresponding to each datapoint in the longitudinal creep curves represent the expanded uncertainty of that point to 95% coverage, where its width represents uncertainty in the longitudinal creepage measurement calculated via Equations (5), (8), and (10) and its height represents the uncertainty in the CoA measurement, calculated via Equations (13) and (14). The black dashed lines, which connect the corners of the shaded regions, show the bounds of the overall uncertainty of the measured creep curves to 95% coverage. We may notice that the error bar length and uncertainty in the vertical direction are small, again suggesting excellent repeatability in the measured CoA values. Considering the error bar scale in the horizontal direction is 1/10 that of the vertical direction, a larger deviation was observed in the longitudinal creepage measurement in comparison to the CoA measurement, because the accuracy of speed measurement was not as high as that of force measurement. The impact of the uncertainty in the longitudinal creepage measurement on the longitudinal creep curves was more prominent in the lower creepage values (below 0.4%), where the initial points are shifted to the right and the black dashed curves are further apart in the figure.

#### 3.2.2. Influence of the Torque Direction

The influence of the direction of the applied torque, either accelerating or braking, can be observed by comparing the longitudinal creep curves obtained from Test 2 and Test 3 at three different wheel rolling speeds. Theoretically, no difference in the creep curves is expected between the traction and braking conditions [2]. This is confirmed by the measurement results shown in Figure 13, where Test 2 and Test 3 provided quite similar trends of the creep curves. A larger scatter of datapoints can be noticed in Figure 13c for the test cases at the speed of 16 km/h. This is because the structural vibrations of the V-Track at high speeds may affect the wheel angular speeds $\omega_0$ and $\omega$, which were used to calculate the longitudinal creepage via Equation (4). In this study, the scattered measurement data obtained from the higher-speed test cases could still provide reasonable trends of the longitudinal creep curve, which could be confirmed when compared to the theoretical results in Section 3.2.4. In future studies, if "smoother" creep curves are to be measured, the wheel–rail interface irregularities should be reduced to mitigate contact-induced structural vibrations.

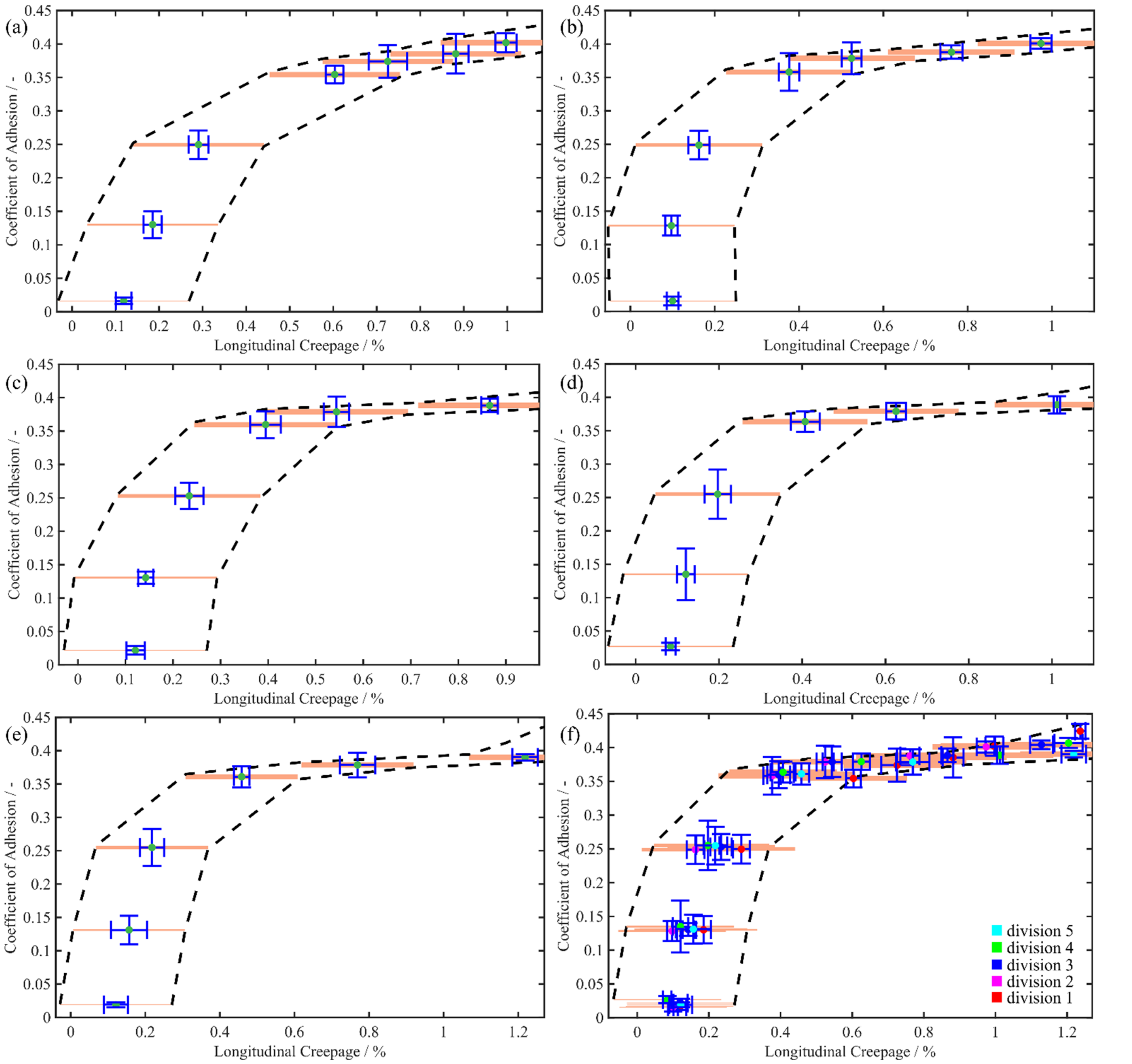


**Figure 12.** Longitudinal creep curves for Test 2 v8: (**a**) division 1; (**b**) division 2; (**c**) division 3; (**d**) division 4; (**e**) division 5; (**f**) comparing creep curves of all divisions.

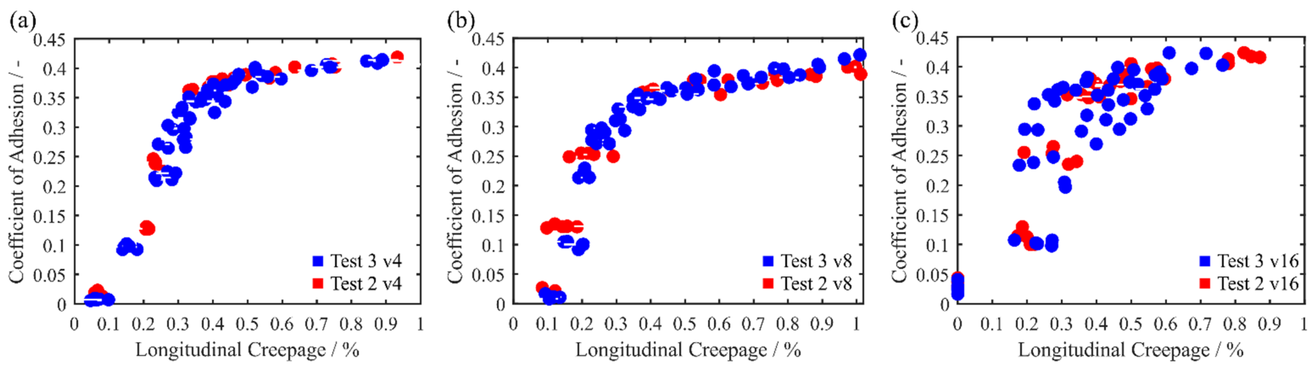


**Figure 13.** Comparison between the longitudinal creep curves from Test 2 (braking) and Test 3 (accelerating) across all the tested speeds: (**a**) 4 km/h; (**b**) 8 km/h; (**c**) 16 km/h.

3.2.3. Influence of the Rolling Speed

The longitudinal creep curves measured with different speeds are compared in Figure 14 to examine the influence of the wheel rolling speed on the longitudinal creep curve. For both the braking and accelerating cases, shown in Figures 14a and 14b, respectively, we can see that the measured datapoints become more scattered when the speed is increased due to the structural vibrations of the V-Track as mentioned above. We do not see either the CoF or creep coefficient decreasing with the increase in wheel speeds, as observed in the lateral creep curve measurement. Regarding the CoF, this could be because the speed dependence of the CoF usually occurs at high values of the absolute sliding speed (>1 m/s) [35], and with the rolling speeds (<16 km/h) and longitudinal creepage values (<1%) used in this study, the absolute sliding speed only reached a maximum of 0.045 m/s. At these levels, the influence of the rolling speed on the longitudinal creep curve may be negligible, as reported in [4,11]. This leads to an interesting finding that the lateral creep curve could be more sensitive to the influence of the rolling speed than the longitudinal one. Regarding the creep coefficient, since it relies on the accurate measurement of the longitudinal creepage, especially at the low creepage range (<0.4%), it can be further studied in the future with the implementation of a high-precision encoder onto the V-Track.

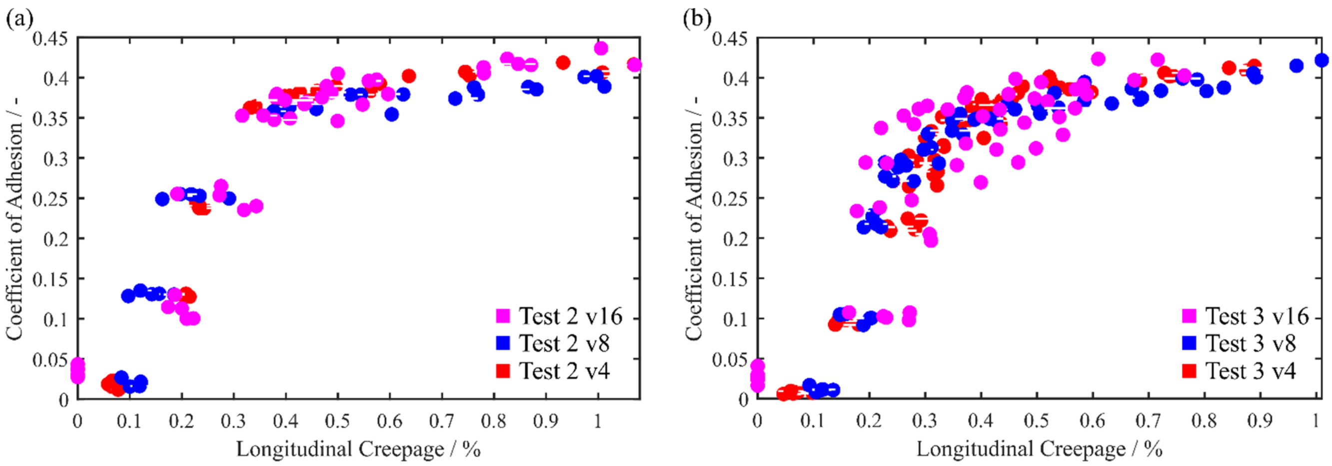


**Figure 14.** Comparison between the longitudinal creep curves across tested speeds: (**a**) Test 2 (braking); (**b**) Test 3 (accelerating).

3.2.4. Comparison with CONTACT

The measured longitudinal creep curves at all three wheel rolling speeds were compared against the theoretical longitudinal creep curves predicted by Kalker's CONTACT in Figure 15 for Test 2 and in Figure 16 for Test 3. Reasonable agreement was achieved between the measurements and the simulations, especially when the longitudinal creepage was above 0.3%. The discrepancies below 0.3% were, again, due to the uncertainty of the wheel angular speed measurement in the current setup. Although the measured datapoints became more scattered with the increase in speed, the CONTACT curves appear to be good fits for the points. This demonstrates the V-Track test rig as a reliable tool for wheel–rail longitudinal creep curve measurements.

### *3.3. Comparison Between the Longitudinal and Lateral Creep Curves*

In principle, considering wheel and rail as isotropic materials, a pure longitudinal creep curve and a pure lateral creep curve obtained with the same contact geometry, contact body material, and normal load may saturate at the same CoF value [2]. In this study, the lateral and longitudinal creep curve tests were independently measured using the V-Track with different experimental principles. The lateral creep curve tests were displacement-controlled, with an independent variable of the AoA, while the longitudinal creep curve tests were force-controlled, with an independent variable of torque. The measured lateral creep curves were compared with longitudinal creep curves obtained from both the braking and accelerating tests in Figures 17 and 18, respectively, across all the tested speeds. The averages of the maximum CoA values measured across all five rail divisions were regarded as the measured CoFs. The location of the CoF value corresponding to each creep curve is also indicated in Figures 17 and 18, using a yellow marker for the longitudinal creep curves and a cyan marker for the lateral creep curves. With a cross-check of the measured CoFs tabulated in Table 3, we obtained a reasonable agreement, with an approximate percentage difference of only 2.5% for speeds below 16 km/h. This also shows the reliability and accuracy of the V-Track for the CoF measurement. A maximum percentage difference of 8.55% at the speed of 16 km/h could be attributed to the increased sensitivity of the lateral creep curve to the wheel rolling speed as discussed in Section 3.2.3. This will be further investigated in the future using the upgraded V-Track.

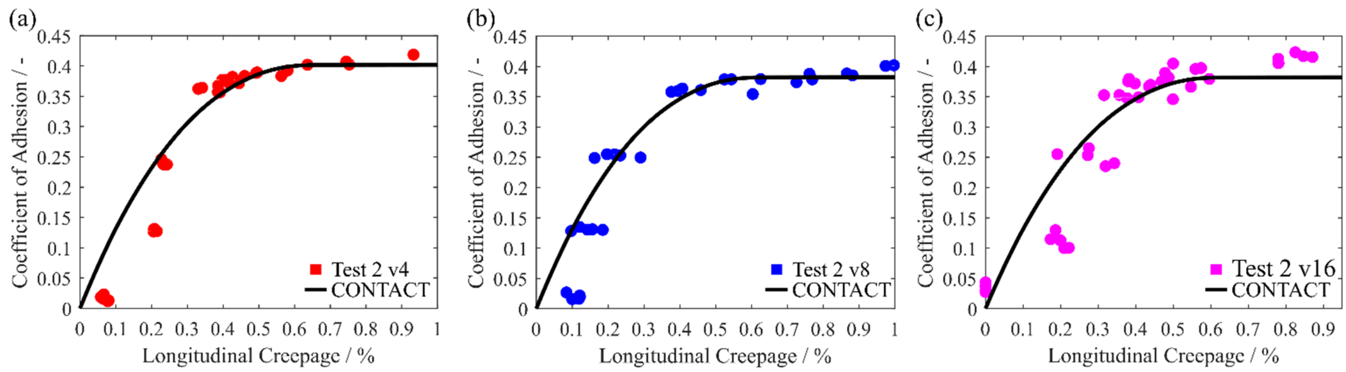


**Figure 15.** Comparison between the measured longitudinal creep curves from braking tests and the numerical longitudinal creep curves from Kalker's CONTACT: (**a**) Test 2 v4; (**b**) Test 2 v8; (**c**) Test 2 v16.

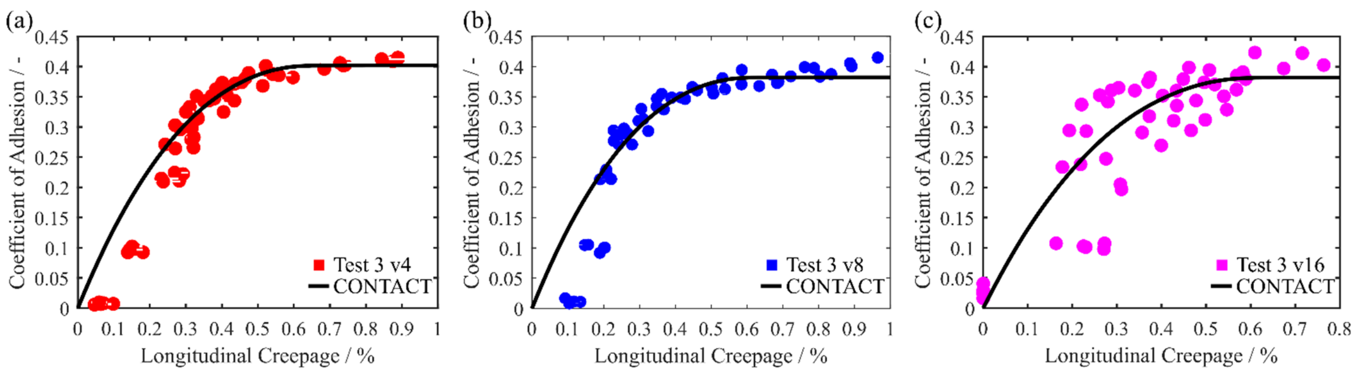


**Figure 16.** Comparison between the measured longitudinal creep curves from accelerating tests and the numerical longitudinal creep curves from Kalker's CONTACT: (**a**) Test 3 v4; (**b**) Test 3 v8; (**c**) Test 3 v16.

**Table 3.** Comparison of the CoF values from lateral and longitudinal creep curves.

| Wheel Translational Speed | Test 1 | Test 2 | Test 3 | Percentage Difference, Test 1 vs. Test 2 | Percentage Difference, Test 1 vs. Test 3 |
|---|---|---|---|---|---|
| 4 km/h | 0.4021 | 0.4113 | 0.4111 | 2.2879 | 2.2382 |
| 8 km/h | 0.3823 | 0.3917 | 0.3924 | 2.4588 | 2.6419 |
| 16 km/h | 0.3822 | 0.4149 | 0.4080 | 8.5557 | 6.7504 |

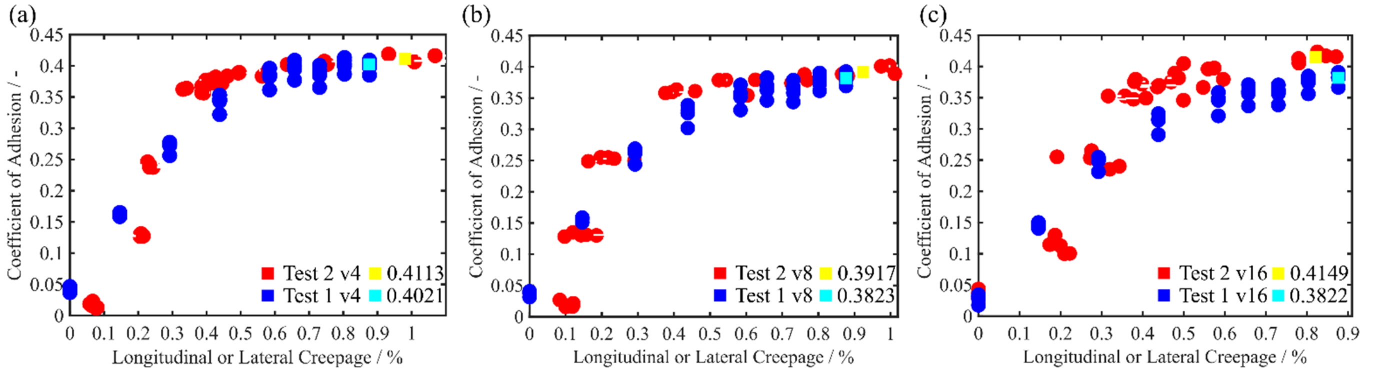


**Figure 17.** Comparison between the lateral creep curves and the longitudinal creep curves from the braking tests across all the tested speeds: (**a**) 4 km/h; (**b**) 8 km/h; (**c**) 16 km/h.

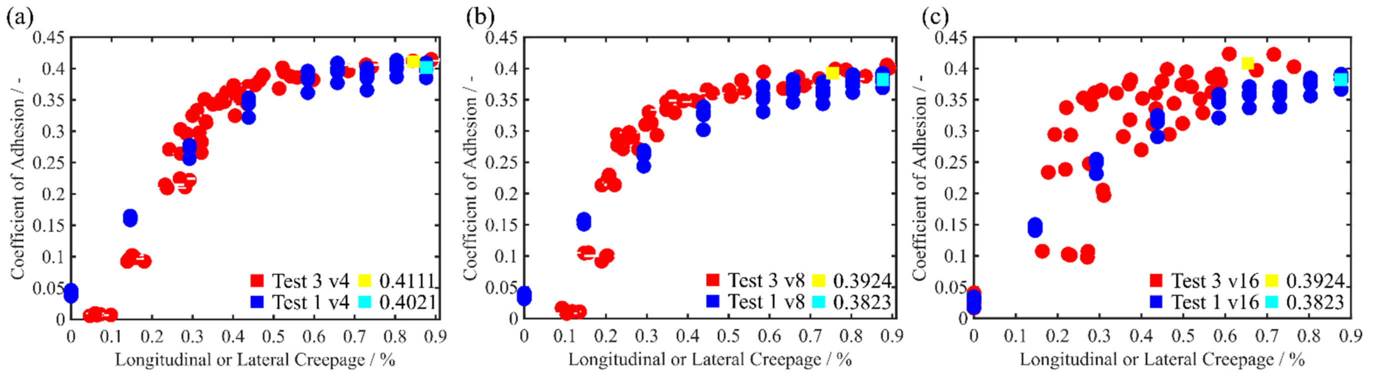


**Figure 18.** Comparison between the lateral creep curves and the longitudinal creep curves from the accelerating tests across all the tested speeds: (**a**) 4 km/h; (**b**) 8 km/h; (**c**) 16 km/h.

## 4. Conclusions and Future Work

The V-Track test rig was employed in this study to measure the wheel–rail lateral and longitudinal creep curves under clean and dry contact conditions. The novel contributions from this study are threefold. 1. With proper representations of train/track components, the V-Track tests revealed the effects of structural dynamics on measuring wheel–rail creep curves in real life through the increased variability in creepage measurements. 2. Pure lateral and longitudinal creepage conditions were produced with two distinct experimental principles—displacement- and force-controlled—on the V-Track, i.e., by carefully controlling the angle of attack and the traction/braking torque, respectively, and thus the coefficients of friction from lateral and longitudinal creep curves measured on the same platform were cross-checked. 3. The uncertainties in the measured creep curves were analysed, and the creep curves were plotted with the corresponding expanded uncertainty ranges; this was rarely addressed in previous studies on creep curve measurement. The conclusions from the comparison of the measured and theoretical creep curves and the sensitivity study are as follows:

1. For the lateral creep curve: the lateral creep curve tests indicate a slight decrease in the CoF value and a reduction in the creep coefficient with the increase in the wheel rolling speed. The CoF decrease with speed was in line with previous studies, while the creep coefficient reduction was probably induced by the debris of the wheel/rail material acting as a third-body layer at the wheel–rail interface for the higher-speed test cases. Excellent agreement was achieved between the experimental and theoretical lateral creep curves. Small discrepancies were found in the higher-speed test cases because the applied CONTACT programme does not consider the effect of third-body layers.

2. For the longitudinal creep curve: the longitudinal creep curves measured with the accelerating and braking torques showed quite similar trends, corresponding well to the theoretical results. The speed dependence of the CoF that is often observed with high values of the absolute sliding speed (>1 m/s) did not occur in this study, possibly because the rolling speeds (<16 km/h) and the longitudinal creepage (<1%) values applied in this study produced sliding speeds not higher than 0.045 m/s. Good agreement was achieved between the measured and simulated longitudinal creep curves, especially when the longitudinal creepage was above 0.3%. The discrepancies below 0.3% could be due to the uncertainty of the wheel angular speed measurement in the current test setup.
3. The agreement between the experimental and theoretical results, as well as the aligned CoFs measured with the lateral and longitudinal creep curve tests, demonstrated the reliability of the V-Track for wheel–rail creep curve measurements and its suitability for studying the wheel–rail frictional rolling contact.

The limitations of the study present opportunities for enhancement and further research. Relatively high measurement uncertainties suggest that the creep curve measurement at low longitudinal creepage values can be improved. Additionally, the pre-set AoA was assumed to remain constant throughout the complete ring track circumference. Further research may focus on reducing measurement uncertainty by implementing higher-resolution encoders and a continuous AoA monitoring system. Better control of wheel–rail surface irregularities is also needed to minimise the contact-induced structural vibrations that affect measurement stability at high speed. The upgraded V-Track will then be used to investigate creep curve characteristics under more complex friction conditions, such as in the presence of water contamination, leaf layer deposits, lubricants, and friction modifier applications.

**Author Contributions:** Conceptualization: Z.Y. and G.J.K.; methodology: J.M., G.J.K. and Z.Y.; formal analysis: G.J.K., Z.Y. and Z.L.; investigation: G.J.K.; resources: Z.L.; writing—original draft preparation: G.J.K.; writing—review and editing: Z.Y. and Z.L.; supervision: Z.Y. and Z.L.; funding acquisition: Z.L. All authors have read and agreed to the published version of the manuscript.

**Funding:** This research was partly supported by ProRail and Europe's Rail Flagship Project IAM4RAIL—Holistic and Integrated Asset Management for Europe's RAIL System. Funded by the European Union. Views and opinion expressed are, however, those of the authors(s) only and do not necessarily reflect those of the European Union. Neither the European Union nor the granting authority can be held responsible for them. This project has received funding from the European Union's Horizon Europe research and innovation programme under Grant Agreement No. 101101966.

**Data Availability Statement:** The datasets presented in this article are not readily available because the data are part of an ongoing study. Requests to access the datasets should be directed to the corresponding author.

**Conflicts of Interest:** The authors declare no conflicts of interest. The funders had no role in the design of the study; in the collection, analyses, or interpretation of data; in the writing of the manuscript; or in the decision to publish the results.

## References

1. Fletcher, D.I.; Lewis, S. Creep Curve Measurement to Support Wear and Adhesion Modelling, Using a Continuously Variable Creep Twin Disc Machine. *Wear* **2013**, *298–299*, 57–65. [CrossRef]
2. Kalker, J.J. *Three-Dimensional Elastic Bodies in Rolling Contact*; Springer Nature: Dordrecht, The Netherlands, 1990. [CrossRef]
3. Tanimoto, H.; Chen, H. Influence of Surface Roughness and Temperature on Wheel/Rail Adhesion in Wet Conditions. *Q. Rep. RTRI* **2015**, *56*, 206–211. [CrossRef]
4. Zhang, W.; Chen, J.; Wu, X.; Jin, X. Wheel/rail Adhesion and Analysis by Using Full Scale Roller Rig. *Wear* **2002**, *253*, 82–88. [CrossRef]

5. Li, Z.; Arias-Cuevas, O.; Lewis, R.; Gallardo-Hernández, E.A. Rolling–Sliding Laboratory Tests of Friction Modifiers in Leaf Contaminated Wheel–Rail Contacts. *Tribol. Lett.* **2009**, *33*, 97–109. [CrossRef]
6. Chen, Q.; Ge, X.; Shi, Z.; Ling, L.; Hu, X.; Hu, Y.; Wang, K. Measurement of Vehicle Speed Based on the GCC Algorithm and its Application in Anti-Slip Control. *Measurement* **2023**, *219*, 113298. [CrossRef]
7. Pichlik, P.; Bauer, J. Analysis of the Locomotive Wheel Slip Controller Operation During Low Velocity. *IEEE Trans. Intell. Transp. Syst.* **2021**, *22*, 1543–1552. [CrossRef]
8. Engelberg, T. Design of a Correlation System for Speed Measurement of Rail Vehicles. *Measurement* **2001**, *29*, 157–164. [CrossRef]
9. Giner, J.; Baeza, L.; Vila, P.; Alonso, A. Study of the Falling Friction Effect on Rolling Contact Parameters. *Tribol. Lett.* **2017**, *65*, 29. [CrossRef]
10. Briales, E.; Urda, P.; Escalona, J.L. Track Frame Approach for Heading and Attitude Estimation in Operating Railways Using On-Board MEMS Sensor and Encoder. *Measurement* **2021**, *184*, 109898. [CrossRef]
11. Alonso, A.; Guiral, A.; Baeza, L.; Iwnicki, S. Wheel–Rail Contact: Experimental Study of the Creep Forces–Creepage Relationships. *Veh. Syst. Dyn.* **2014**, *52*, 469–487. [CrossRef]
12. Gutsulyak, D.V.; Stanlake, L.J.E.; Qi, H. Twin Disc Evaluation of Third Body Materials in the Wheel/Rail Interface. *Tribol.-Mater. Surf. Interfaces* **2021**, *15*, 115–126. [CrossRef]
13. Ahn, K.; Park, J.; Ryew, S. The Construction of a Full-Scale Wheel/Rail Roller Rig in Korea. In Proceedings of the 2012 IEEE International Conference on Automation Science and Engineering (CASE), Seoul, Republic of Korea, 20–24 August 2012; IEEE: Piscataway, NJ, USA, 2012; pp. 802–803. [CrossRef]
14. Boyacioglu, P.; Bevan, A.; Allen, P.; Bryce, B.; Foulkes, S. Wheel Wear Performance Assessment and Model Validation Using Harold Full Scale Test Rig. *Proc. Inst. Mech. Eng. Part F J. Rail Rapid Transit* **2022**, *236*, 406–417. [CrossRef]
15. Meymand, S.Z.; Ahmadian, M. Design, Development, and Calibration of a Force-Moment Measurement System for Wheel–Rail Contact Mechanics in Roller Rigs. *Measurement* **2016**, *81*, 113–122. [CrossRef]
16. Radmehr, A.; Hosseinian Ahangarnejad, A.; Tajaddini, A.; Ahmadian, M. Investigating the Influence of Angle of Attack (Yaw) on Wheel-Rail Interface (WRI) Dynamics. In Proceedings of the 2020 Joint Rail Conference, American Society of Mechanical Engineers, St. Louis, MO, USA, 20–22 April 2020; p. V001T13A003. [CrossRef]
17. Shu, X.; Zeng, Y.; Wilson, N.; Thompson, R.; Tajaddini, A. Wheel/Rail Contact Creep Curve Measurement and Low Speed Wheel Climb Derailment Investigation. In *Advances in Dynamics of Vehicles on Roads and Tracks*; Klomp, M., Bruzelius, F., Nielsen, J., Hillemyr, A., Eds.; Springer International Publishing: Cham, Switzerland, 2020; pp. 660–668. [CrossRef]
18. Liu, X.; Xiao, C.; Meehan, P.A. The Effect of Rolling Speed on Lateral Adhesion at Wheel/Rail Interface Under Dry and Wet Condition. *Wear* **2019**, *438–439*, 203073. [CrossRef]
19. Petersen, D.; Link, R.; Fletcher, D.; Beynon, J. Development of a Machine for Closely Controlled Rolling Contact Fatigue and Wear Testing. *J. Test. Eval.* **2000**, *28*, 267–275. [CrossRef]
20. Naeimi, M.; Li, Z.; Petrov, R.H.; Sietsma, J.; Dollevoet, R. Development of a New Downscale Setup for Wheel-Rail Contact Experiments under Impact Loading Conditions. *Exp. Tech.* **2018**, *42*, 1–17. [CrossRef]
21. Zhang, P.; Moraal, J.; Li, Z. Design, Calibration and Validation of a Wheel-Rail Contact Force Measurement System in V-Track. *Measurement* **2021**, *175*, 109105. [CrossRef]
22. Ren, F.; Yang, Z.; Li, Z. Experimental and Numerical Investigation into Rolling Contact Fatigue Crack Initiation on the V-Track Test Rig. *Eng. Fail. Anal.* **2025**, *170*, 109206. [CrossRef]
23. Zhang, P.; He, C.; Shen, C.; Dollevoet, R.; Li, Z. Comprehensive Validation of Three-Dimensional Finite Element Modelling of Wheel-Rail High-Frequency Interaction via the V-Track Test Rig. *Veh. Syst. Dyn.* **2024**, *62*, 2785–2809. [CrossRef]
24. Krishnan, G.J.; Yang, Z.; Li, Z. Wheel/Rail Adhesion and Coefficient of Friction Measurement using Downscaled Test Rig. In Proceedings of the Sixth International Conference on Railway Technology: Research, Development and Maintenance, Prague, Czech Republic, 1–5 September 2024; Pombo, J., Ed.; Online volume: CCC 7, Paper 2.5. Civil-Comp Press: Edinburgh, UK, 2024. [CrossRef]
25. Guides in Metrology. JCGM. 2008. Evaluation of Measurement Data—Guide to the Expression of Uncertainty in Measurement. Available online: https://www.bipm.org/documents/20126/2071204/JCGM_100_2008_E.pdf/cb0ef43f-baa5-11cf-3f85-4dcd86f77bd6 (accessed on 23 June 2025).
26. Kavanagh, R. Improved Digital Tachometer with Reduced Sensitivity to Sensor Nonideality. *IEEE Trans. Ind. Electron.* **2000**, *47*, 890–897. [CrossRef]
27. Prieto, E.; del Mar Pérez, M.; Yandayan, T.; Przybylska, J.; Just, A.; Geckeler, R. Guidelines on the Calibration of Angular Encoders. 2018. Available online: https://www.euramet.org/Media/news/I-CAL-GUI-023_Calibration_Guide_No._23_web.pdf (accessed on 23 June 2025).
28. Avago Technologies. HEDM-55xx/560x & HEDS-55xx/56xx. Quick Assembly Two and Three Channel Optical Encoders Data Sheet. Available online: https://hades.mech.northwestern.edu/images/d/d7/HEDS5500-encoder.pdf (accessed on 23 June 2025).

29. Hace, A.; Čurkovič, M. Accurate FPGA-Based Velocity Measurement with an Incremental Encoder by a Fast Generalized Divisionless MT-Type Algorithm. *Sensors* **2018**, *18*, 3250. [CrossRef] [PubMed]
30. Avago Technologies. HEDS-51X0/61X0 Series, HEDG-512X/612X Series HEDM-512X/61XX Series Two and Three Channel Codewheels for Use with Avago Technologies Optical Encoder Modules Technical Data. Available online: https://www.mouser.com/datasheet/2/38/V02-1450EN-107271.pdf?srsltid=AfmBOoqwyvsbxOHdvkm8F2RLrBlHsOt___mmPzTu6OHdr_1gegtcN55a (accessed on 23 June 2025).
31. Aguado-Rojas, M.; Pasillas-Lépine, W.; Loría, A.; De Bernardinis, A. Angular velocity estimation from incremental encoder measurements in the presence of sensor imperfections. *IFAC-PapersOnLine* **2017**, *50*, 5979–5984. [CrossRef]
32. Gallardo-Hernandez, E.; Lewis, R. Twin Disc Assessment of Wheel/Rail Adhesion. *Wear* **2008**, *265*, 1309–1316. [CrossRef]
33. Monk-Steel, A.; Thompson, D.; de Beer, F.; Janssens, M. An Investigation into the Influence of Longitudinal Creepage on Railway Squeal Noise due to Lateral Creepage. *J. Sound Vib.* **2006**, *293*, 766–776. [CrossRef]
34. Fletcher, D. A New Two-Dimensional Model of Rolling–Sliding Contact Creep Curves for a Range of Lubrication Types. *Proc. Inst. Mech. Eng. Part J J. Eng. Tribol.* **2013**, *227*, 529–537. [CrossRef]
35. Vollebregt, E.; Six, K.; Polach, O. Challenges and Progress in the Understanding and Modelling of the Wheel–Rail Creep Forces. *Veh. Syst. Dyn.* **2021**, *59*, 1026–1068. [CrossRef]